Application of the elliptic approximation model for the edge turbulence rotation measurement via the poloidal correlation reflectometer in Wendelstein 7-X

X Han[1,2], A Krämer-Flecken[2], H M Xiang[1,2], M Vécsei[3], A Knieps[2], T. Windisch[4], G Anda[3], T Andreeva[4], S A Bozhenkov[4], J Geiger[4], D Dunai[3], E Trier[5], K Rahbarnia[4], S Zoletnik[3], Y. Liang[2], and the W7-X team[4] ‡

[1] Institute of Plasma Physics, Chinese Academy of Sciences, 230031 Hefei, Anhui, People's Republic of China

[2] Forschungszentrum Jülich GmbH, Institute für Energie-und Klimaforschung - Plasmaphysik, Partner of the Trilateral euregio Cluster (TEC), 52425 Jülich, Germany

[3] Centre for Energy Research, 1525 Budapest, Hungary

[4] Max-Planck-Institut für Plasmaphysik, 17491 Greifswald, Germany

[5] Max-Planck-Institut für Plasmaphysik, 85748 Garching, Germany

E-mail: xi.han@fz-juelich.de

Abstract. The perpendicular velocity ($v_\perp$) of turbulence is measured by means of a hopping poloidal correlation reflectometer diagnostic for the study of turbulence rotation in the plasma edge region in Wendelstein 7-X. An elliptic approximation (EA) model is applied for calculating the space-time correlation in the edge region. The $v_\perp$ profile is compared in the high-ι (edge $\iota \approx 1.2$) and limiter (edge $\iota < 1$) configurations. It is found that the $v_\perp$ gradient is inversely proportional to the heating power in the high-ι configuration, which could be attributed to the turbulence activities in the plasma edge. In the limiter configuration, the $v_\perp$ spike is observed near the island boundary, which is corresponded to the plasma current crash. In the standard configuration (edge $\iota \approx 1$), the $v_\perp$ profile in the island region distributes as a function of the perpendicular separation. With increasing of the plasma current, the island enlarges the size as is referred from the $v_\perp$ scope, accompanying with steepening of the $v_\perp$ gradient at the boundary of the island.

Keywords: turbulent perpendicular velocity, elliptic approximation model, shear flow

Submitted to: *Nucl. Fusion*

‡ Members of the W7-X team are listed in Wolf *et al* [1].

1. Introduction

Measurement of the turbulence rotation in the vicinity of the shear layer is one of the attractive and crucial issues in the magnetic confinement device since it allows a better understanding of the anomalous transport in the plasma edge region and hence the improvement of overall confinement[2]. The space-time correlation has been used for the turbulence rotation measurement, which detects the turbulent flow as it passing across two spatially separated positions, the fluctuation patterns reveals a similarity within a certain time delay. The velocity for describing the turbulence propagation can be derived from a measured time delay and the separation between two positions. This space-time correlation method is defined as the Taylor's frozen-flow hypothesis[3], and is satisfied if two positions are close to each other compared to the turbulent correlation length and decorrelation time. The space-time correlation is demonstrated approximately by a time delay and a constant speed for the turbulence flow propagation. Various diagnostics have proven their capabilities of measuring the turbulence rotation based on the ahead mentioned model[4, 5].

In the magnetic-confined plasma, the $\mathbf{E} \times \mathbf{B}$ velocity shear plays a key role on the turbulence reduction by modifying the turbulent eddy's growth rate and its radial extent[6], hence the eddy structure is torn apart as it approaches the shear layer. The Taylor's hypothesis is valid under the condition of a weak shear rate and low turbulence intensity[7, 8]. However, it becomes less applicable especially in the vicinity of a shear region where the radial change of $\mathbf{E} \times \mathbf{B}$ flow becomes significant. In such case, the measured space-time correlation contains the information from the radial extension of the turbulent eddy, yielding a two-peaks structure in the cross-correlation function (CCF) [9], the Taylor's hypothesis results in an infinite velocity in the shear layer. The limitation becomes more severe if the poloidal separation of two positions is enlarged. The assumptions are no longer fulfilled in the Taylor's hypothesis since where the turbulence radial propagation is represented by a mean flow without any degradation of the turbulence size, the decorrelation process of the radial extension of small-scale eddy is not taken into account. In fact, the turbulent eddy is supposed to be stabilized by the $\mathbf{E} \times \mathbf{B}$ shear effect. The poloidal rotation of the radial extended eddies tends to be zero when the eddy approaches the shear layer. Then eddies are accelerated in the opposite direction[10].

An elliptic approximation (EA) has been developed earlier for illustrating the turbulence rotation in the shear layer. It is invented for the purpose to explain the radio-wave fading process in the ionosphere[11]. It has been introduced to the neutral shear flow[12] studies, as well as the fluid instabilities in the magnetized plasma[13]. The basic idea of EA model is that the space-time correlation for a dispersive propagating turbulence follows the distribution where the correlation maxima appears at the initial position and declines as a function of both time and spatial separations. The iso-correlation contour of the turbulent flow forms an elliptical shape, which shares a common preference direction and aspect ratio. From the mathematical point of view, the elliptical shape of the iso-correlation contour can be proved by expanding the correlation function in a Taylor power series to its second order, whereas the Taylor's model is the linear approximation[14]. The EA model is a more complete description to investigate the

turbulence propagation in a shear flow since it considers the physical nature of the turbulence alteration into account.

In this paper, we are going to apply the EA model for measuring the poloidal rotation of the turbulence, which direction is perpendicular to magnetic field line ($v_\perp$) in the plasma edge region of a poloidal cross section in Wendelstein 7-X (W7-X). W7-X is an optimized stellarator aiming for the reduction of neoclassical transport by means of the three-dimensional geometry of magnetic field to achieve a quasi-isodynamic equilibrium at high plasma beta regime[15, 16]. The experimental measurement is performed by a poloidal correlation reflectometer diagnostic (PCR)[17, 18, 19], which is installed in a bean-shaped plasma cross-section for the purpose of investigation on the turbulence behavior at the interface between edge and core plasmas[20].

The $v_\perp$ measurement by PCR is validated on ASDEX Upgrade, where the $v_\perp$ is compared with the Doppler reflectometer (DR) measurements. Result shows a reasonable agreement in the plasma edge[21]. On W7-X, the $v_\perp$ can be estimated via the triple-probe model by a set of Langmuir manipulator (MPM) in a different cross section[22]. It is observed that the $v_\perp$ agrees with the PCR measurement [19] in the scrap-off layer (SOL) region. The Doppler reflectometer (DR) system, which locates at the same cross-section of PCR, can measure the $v_\perp$ profile as well. the inversion of $v_\perp$ has been observed in the plasma edge region via the DR measurement[23], yielding a clear dependence of the edge shear on heating power and density. However, the $v_\perp$ comparison with DR measurement is not possible since the DR is operated in W-band (75-110 GHz) in X-mode regime, which has no common radial coverage with the PCR measurement.

To measure the $V_\perp$ profile via PCR, the electron density (n_e) profile is necessary in order to locate the cutoff position of each probing frequency. In OP1.1 and 1.2a campaigns, the n_e profile is obtained from the Thomson Scattering (TS)[24, 25] measurement. However, uncertainty arises when determining the cutoff position in the SOL due to the of difference cross sections in PCR (bean-shape) and TS (triangular shape). The problem becomes significant in the standard configuration as the PCR and TS line of sights (LoS) intersects with the 5/5 island structure in different views[26, 27]. The TS's LoS is closer to the X-point of island, whereas the PCR's one is closer to the O-point. In OP1.2b campaign, this problem is solved by measuring the n_e profile near the PCR's LoS via the Alkali beam emission spectroscopy diagnostic (ABES) [28]. In the following analysis, the measurement is presented by the ABES n_e profile for calculating the corresponding cutoff position at plasma edge region of W7-X.

The remaining content of this paper is organized as below: in section 2 the methodology of the EA model is described. In section 3 the PCR setup in W7-X is introduced, the necessary procedure on how to map the n_e profile from the ABES to PCR LoS is illustrated. In section 4 the EA model for the $v_\perp$ estimation is applied in different configurations via the PCR measurement. It is found the $V_\perp$ gradient is inversely proportional to the heating power in the high-ι configuration, which could be attributed to the turbulence activities in the plasma edge. In the limiter configuration, the $V_\perp$ oscillation is observed near the island region as a response to the plasma current crash. In the standard configuration (edge $\iota \approx 1$), the $V_\perp$ profile in the island region is analyzed. In section 5 the current work is summarized.

2. Methodology

Taylor's frozen-flow hypothesis considers a spatial pattern of the turbulent flow that propagates poloidally in a constant speed U without any essential change. The CCF of two discrete complex signals $E_1(\xi, t)$ and $E_2(\xi + \delta\xi, t)$, which are vertically separated on the poloidal plane, is defined to be:

$$\Gamma(\delta\xi, \tau) = \frac{\sum_i E_1(\xi, t_i) \cdot E_2^*(\xi + \delta\xi, t_i + \tau)}{\sqrt{\sum_i E_1(\xi, t_i)^2 \cdot E_2(\xi + \delta\xi, t_i + \tau)^2}} \quad (1)$$

where the ensemble averaging is performed over a certain time series of interest, and τ is the time delay between the two signals. Hence the space-time correlation of the turbulent flow can be expressed by the space correlation and a common speed, i.e., $\Gamma(\xi + \delta\xi, \tau + \delta\tau) = \Gamma(\xi - U\delta\tau, \tau)$. The turbulence velocity is given by the ratio of the space-time separation as $U = \delta\xi/\delta\tau$. This model is applicable if the turbulence level is low and the mean shear is small so that the turbulence perturbation can be neglected[29].

In the shear region the turbulent eddy is elongated[30], the turbulent rotation is gradually degenerated as it approaches the shear layer, and the rotation reverses the direction in the other side of the shear layer. Hence in Taylor's hypothesis the structure of the parallel line in a common velocity is collapsed. In such case the EA model is valid to illustrate the turbulent flow in the shear layer. As is shown in figure 1 the space-time correlation has its maximum at the origin and reduces as the space and time separations increase, that results in an inclined ellipse curve on the iso-correlation contour. The preference direction and aspect ratio of the ellipse are determined by the magnetic field pitch angle ($\tan\alpha$) and the nature of turbulence respectively. With a spatial separation of $\delta\xi$ along the direction perpendicular to the magnetic field, the $\Gamma(\xi, \tau)$ for a single turbulent eddy structure can be described by a Gaussian function on the ξ or τ plane with its maximum at $\tau = 0$ and $\xi = 0$ individually.

In figure 2(a) the CCF profile distributes as a function of the space separation of $\xi_\perp$. The auto-correlation function (ACF) profile is represented by the blue curve where $\xi_\perp = 0$ is satisfied. Figure 2(b) shows the iso-correlation contour of a turbulence flow in the shear layer. The ellipse at the space separation of ξ_1 has its maximum CCF at the time delay of τ_m, which corresponds to the point of the horizontal tangent on the ellipse. One can always find the point of $\Gamma(0, \tau)$ where the ellipse intersects with the $\xi = 0$ axis at the time delay of τ_0, which is referred to the value on the ACF for the equal correlation coefficient to $\Gamma(\xi_1, \tau_m)$, as is shown in the figure 2(a). Therefore the CCF for a turbulence flow is linked to the ACF on the iso-correlation contour by $\Gamma(\xi_1, \tau_m) = \Gamma(0, \tau_0)$. The apparent velocity is defined to be:

$$v_a = \xi_1/\tau_m \quad (2)$$

. The v_a follows the preference direction on the ellipse, which appears at the first glance to be the velocity of turbulence pattern motion, and is the same to the speed given by the Taylor's hypothesis.

The drift velocity, which is derived from the EA model for describing the actual movement of the turbulence pattern, is given by:

$$v_{drift} = \xi_1\tau_m/(\tau_0^2 + \tau_m^2) \quad (3)$$

. It describes the turbulence pattern propagation that experiences the slowest possible degradation when it passes through the space-arranged detectors. The procedure on how to obtain v_{drift} can be found in the reference [11, 13].

The fading velocity is introduced from the ionosphere radio-waves measurement, and is defined to be:

$$v_{fading} = \xi_1/(\tau_0^2 + \tau_m^2)^{1/2} \quad (4)$$

. It explains the rate at which the turbulence pattern deforms as it moves. One can easily deduce a relation that

$$v_a \times v_{drift} = v_{fading}^2 \quad (5)$$

Two extreme cases should be discussed. (i) $\tau_0 \ll \tau_m$, this may occur when the ACF is much narrower than the CCF, or the space separation is so large that the τ_0 is ignored. In equation 3 it is obtained that $v_{drift} \approx \xi_1/\tau_m = v_a$, and $v_{fading} \approx \xi_1/\tau_m = v_a$. (ii) $\tau_0 \approx \tau_m$, this may happen when the space separation is too small that the preference direction of the contour tends to be vertical to the τ-axis. The velocity is calculated to be $v_{drift} \approx \xi_1/2\tau_m = v_a/2$, and $v_{fading} \approx \xi_1/\sqrt{2}\tau_m = v_a/\sqrt{2}$.

3. Experimental setup in W7-X

The antenna array of PCR, which consists of one launcher and 4 receivers, is installed slightly below the equatorial plane in the bean-shaped cross-section. As seen in the figure 3(a) of the Poincaré figure in the standard configuration, a 5/5 island chain is designed by the magnetic coils module in the open-field line region, the island at the outboard side mid-plane is positioned in front of the PCR LoS. The 4 receivers of PCR are surrounded the launcher (labeled as A) in the following order: the receivers B and C locates at the same poloidal cross-section of A, the receivers D and E are mounted poloidally in the adjacent cross-section. The poloidal and toroidal separations with this antenna array enable the PCR for a 2-dimensional frame of n_e fluctuation measurement.

The PCR operates in a frequency range of 22 to 40 GHz in an ordinary polarization (O-mode), which corresponds to a cutoff n_e of $0.6 \sim 2.0 \times 10^{19}$ m^{-3}. The perpendicular velocity ($v_\perp$) of low-k turbulence ($k_\perp \leq 2$ cm^{-1}) can be measured via PCR. The $v_\perp$ is a combination of the $\mathbf{E} \times \mathbf{B}$ velocity ($v_{E\times B}$), and the phase velocity of turbulence (v_{phase}). In the case of v_{phase} is ignorable, $v_\perp \approx v_{E\times B} = v_{drift}$ is obtained. Therefore the v_{drift} can be represented for the speed of the turbulence flow. According to the equation 3 the perpendicular distance ($\xi_\perp$) is necessary. By applying a multi-point time delay measurement with different poloidal and toloidal separations to extract the magnetic pitch angle on the corresponding flux surface, the drift velocity can be estimated[31]. A ray tracing code based on the two-dimensional full-wave modeling is applied for calculating the distance[32]. In order to include the dominant turbulence contribution to the $v_\perp$ while neglect the DC component, a band-pass filter is necessary to the PCR signal when calculates the CCF and ACF. The filter bandwidth can change the width of CCF and ACF, which would alter the τ_0 value and hence the $v_\perp$ result as shown in the equation 3. The filter bandwidth is determined by the cross-phase spectrum, within which a clear slope of cross-phase is identified. In the following analysis, a band-pass filter of 5 kHz to 1.5 MHz is applied to the PCR signal, this fiter bandwidth is thought to be more than enough to cover the density fluctuation that measured. In case of the particular turbulent mode structure exists, for example a quasi-coherent mode (QC-mode) at 10 to 25kHz or the filament structure[33] that observed in the edge region, it may have a different phase velocity, yielding a side slope structure in the vicinity of the dominant peak in CCF. However, the particular turbulent

modes structures doesn't change the maximum CCF value, hence the band-pass filter of 5kHz to 1.5 MHz remains valid to determine the τ_m value in the $v_\perp$ calculation.

In the OP1.2b campaign, the edge n_e profile is measured by the ABES with high spatial and temporal resolutions on the equatorial plane of the same port of PCR. One issue regarding the LoS of PCR and ABES is that ABES crosses the O-point of island, which is above the PCR's LoS. The density profile could be slightly deformed between this two systems concerning the 3-dimensional magnetic curvature and the island structure in W7-X. This issue can be solved by tracing the ABES n_e profile from the equatorial plane to the PCR LoS. Due to the neighboring toroidal angle of $\Delta\Phi = 0.9°$, the tracing procedure is plausible and can be realized via the field line tracer (FLT)[34] in W7-X.

Figure 3 explains on how to map the n_e profile to the PCR-A LoS via FLT in the standard configuration (EJM, edge $\iota \approx 1$). Firstly, the ABES measurements are traced from the bean-shaped cross-section (toroidal angle $\Phi = 72°$, blue diamonds) to the PCR's one ($\Phi = 71.1°$, the yellow triangles). Secondly, the FLT is performed to obtain a Poincaré figure by means of the line-traced positions. It is found in figure 3(a) that the island structure as well as the ABES measurements are shifted downward by about 2 cm. Then the intersections along the PCR-A LoS can be collected on each flux surface of the Poincaré figure, which are indicated by the red-dots in the figure 3(a). By assuming the density level constrains on the same flux surface in the Poincaré figure, one can obtain the mapped n_e profile along the PCR-A LoS, as is shown in figure 3(b). Comparing with the original ABES n_e profile, the mapped n_e profile moves inward due to the curvature of the flux surface, and the n_e gradients in the island region and last-closed flux surface (LCFS) are modified. This is reasonable since the PCR's LoS goes through the island from a different view, which gives rise to a deviate n_e distribution in radius.

One note is that in case of a peaked n_e profile in the island, a hollow region would appear on the inner-side of island, where the PCR is impossible for the measurement due to its O-mode regime. Therefore the cutoff position of PCR jumps from the peak point to the equivalent n_e layer at the inner-side of the flux surface, yielding a gap region for the PCR measurement. This situation happens occasionally in the EJM configuration where the density in the 5/5 island chain can be moderated by the plasma current, and/or the plasma beta during the discharge. In the following sections, the mapped n_e profiles are applied for the analysis of $v_\perp$ profile. The connection length contour shows only a remnant island structure, yet a full island can be seen in the Poincaré figure. This process is due to the fact that the Poincaré figure is obtained by neglecting the divertor module in the calculation. In the realistic case, the divertor module cut the island chain in the SOL resulting in a remnant island structure. Therefore the mapped n_e profile is shifted inward by $5 \sim 8$ mm in order to match the connection length contour. This correction is still within the range of PCR's radial resolution, and can be calibrated once the n_e profile measurement along PCR-A sight line is ready.

4. $V_\perp$ measurements in W7-X

In this section, three examples are presented for the $v_\perp$ estimations via PCR measurements at the plasma edge region in W7-X. The EA

model is applied for the turbulence space-time correlation in the shear layer. (i) In 4.1, in the high-ι (edge $\iota \approx 1.2$) configuration (FTM) $v_\perp$, v_a, and v_{fading} are compared during the heating power scan. It is observed the $v_\perp$ gradient is modified by the heating power. (ii) In 4.2, the $v_\perp$ profiles are compared in the configuration scan. In the limiter configuration (FMM, edge $\iota < 1$), the $v_\perp$ spike near the island boundary is observed as a response of the plasma current crash. (iii) In 4.3, the $v_\perp$ in the island region is studied in the EJM configuration. The $v_\perp$ evolves as the plasma current increases.

4.1. Edge $v_\perp$ profile in ECRH power scan in FTM configuration

Figure 4 presents the time trace of the $v_\perp$ evolution in the ECRH power scan in the FTM configuration, where the PCR hops with a frequency step of 500 MHz and time interval of 20 ms. In each frequency step, the time is equally divided into 4 segments, i.e. the $v_\perp$, v_a, and v_{fading} are calculated every 5 ms so as to improve the resolution. The four receivers of PCR can obtain 6 values through different antenna combinations. It is noticed that the $v_\perp$ value in BD combination is smaller than the others, this may be due to the short poloidal separation compared to the radial resolution, which is proportional to the density scale length L_{n_e}. The time delay measurement for this short distance could be perturbed. Therefore the velocities are averaged among the 5 combinations excluded BD.

It is found that the sign of $v_\perp$ alters from the electron-diamagnetic drift direction ($v_\perp > 0$) to the ion-diamagnetic one ($v_\perp < 0$) repeatedly in each of the PCR sweep cycle, which gives us a hint to distinguish the regions of scrap-off layer (SOL) and plasma edge[19]. The v_a evolves toward infinite in the shear region. The $v_\perp$, on the other hand, shows a smooth transition from positive to the negative when the cutoff position moves through the shear layer. The infinite v_a is caused by only taking the maximum time delay (τ_m) into account, which is not precise for the vicinity of LCFS due to the strong shear effect on changing the size and shape of turbulent eddies, hence an inapplicable region for the Taylor's hypothesis. The $v_\perp$ via the EA model reverses its sign gradually in the shear layer, which is more pronounced since it is not physical to have an infinite turbulence rotation in plasma. The fading velocity v_{fading} increases by a factor of 4 inside the LCFS in every sweep cycle, which could be attributed to the turbulence suppression in the confined region.

Figure 5 compares three $v_\perp$ profiles with respect to the different power steps. Here the $v_\perp$ profile is presented along the PCR-A LoS, the cutoff layer is obtained by mapping the ABES measurement as described in the section 3. It is shown in figure 5(a) that the n_e profile stays constant during the scan, it is slightly higher at $P_{ECRH} = 5$ MW. In the SOL region, $v_\perp \approx 2$ km/s is calculated regardless of the ECRH powers. Inside the LCFS, a shear layer can be seen where the $v_\perp$ changes the sign to the negative. The width of the shear layer can be roughly estimated by the radial extent of the $v_\perp$ slope, $w_{shear} \approx 0.8 \sim 1.4$ cm. The $v_\perp$ gradient is calculated as a function of the radius in the shear layer to be $\nabla v_\perp = dv_\perp/dR$. An inverse proportion between the $\nabla v_\perp$ and P_{ECRH} is found that, $\nabla v_\perp = 1057 \pm 313$ kHz at $P_{ECRH} = 5$ MW, 1275 ± 430 kHz at 2 MW, and 1556 ± 291 kHz at 1 MW. Although the ECRH power modifies the edge n_e profile slightly, the n_e gradient stays almost constant in the power steps. The edge turbulence activities may play a role on the $\nabla v_\perp$ in the power scan.

As is shown in the figure 6(a) for the

cross-power spectrum density (CPSD) of BD combination, at 5 MW step a low frequency fluctuation spectrum appears in the range of 3 $\sim$ 30 kHz in the plasma edge region ($v_\perp < 0$), which indicates that the low frequency turbulence is robust and dominates the CPSD spectrum. The CPSD decreases in the time window of 2 MW power step, the broad band spectrum evolves to a weak turbulence structure between 5 to 15 kHz. At the lowest power step of 1 MW, a coherent mode structure is appeared in the time window of $v_\perp < 0$ inside the LCFS, which frequency is centered at 8 kHz with the 1/e bandwidth of 1.5 kHz. This mode can be seen in the Mirnov spectrum as well. The mode amplitude enhances at the same time window of the CPSD of BD, and the strong correlation coefficient between the PCR and Mirnov signals suggests that the 8 kHz mode is an electromagnetic mode. The decorrelation time for the low frequency turbulence at 5 MW is $\tau_{dc} \approx 6\mu$s, which is smaller than the value in the 1 MW case. However, the growth rate of the instabilities is required, from the modelling point of view, to further investigate the effect of $\mathbf{E} \times \mathbf{B}$ shear on the turbulence, yet the mode study is out of the scope in this paper. In our case, CCF and ACF curves with a bandpass filter range including the 8 kHz mode (5 kHz to 1.5 MHz) remain the same as the ones excluding the 8 kHz mode (10 kHz to 1.5 MHz), indicating that the 8 kHz mode has no effect on the $v_\perp$ calculation using the elliptical approach. Nevertheless, it suggests a possible mechanism for the $v_\perp$ evolution during the ECRH power scan.

4.2. $v_\perp$ comparison in the magnetic configuration scan

In W7-X the modular coil assembly can adjust the magnetic configuration (or the ι profile) flexibly. In order to study the edge ι effect on the $v_\perp$ profile, 4 magnetic configurations are presented, which is named as FMM+252, FOM+252, FQM+252, and FTM+252 separately. The names and corresponding coil currents are listed in the table 1. The LCFS location is designated by the magnetic coil assembly beforehand, which is adjusted in a radial variation from millimeters to a few centimeters. The Poincaré figures and the connection length contours are shown in the figure 7, and the corresponding n_e profiles are listed below. It can be seen that the island structure is located inside the LCFS, the boundary of the island moves toward the plasma core gradually from FMM+252 to FQM+252. In the FTM+252 configuration $\iota > 1$ in the center, the island is invisible in the plasma edge. For a comparison of $v_\perp$ profile, the PCR scan is selected at the similar heating power level and plasma current. The result is presented in the figure 8. As shown by the shaded area of the cutoff n_e range, PCR measurement covers the n_e gradient region in the plasma edge. In the SOL region the $v_\perp$ sustains at an equal level of $v_\perp \approx 2$ km/s for all configurations, whilst at the plasma edge $v_\perp = -8 \sim -7$ km/s in FTM and FQM configurations, which is 2 km/s higher than in FOM and FMM.

In the FOM configuration, the $\nabla v_\perp$ is peaked at around 800 kHz at R = 6.217 m, which is much weaker than the other configurations. However, the width of shear layer in FOM is $w_{shear} \approx 1.0$ cm, that is wider than the other configurations. The different width may be attributed by the

change of the magnetic curvature effect and/or the pressure profiles in the plasma edge region. It is observed that the plasma pressure is the highest in the FMM configuration, yielding an increase of the diamagnetic energy (W_{dia}) and confinement time[35, 36].

Furthermore, in the FMM configuration the total current (I_{tot}) crash occurs regularly, which leads to a transient diamagnetic energy drop of $0.5 \sim 6\%$[37]. The $v_\perp$ spike is observed in the FMM configuration, as shown in figure 8, which is correlated with the I_{tot} crash. This $v_\perp$ spike phenomenon could be explained as the n_e profile relaxation process that is triggered by the I_{tot} crash. As indicated by the vertical dashed lines in figure 9, the variation of the $v_\perp$ is $\Delta v_\perp \approx 2\ km/s$ with respect to a current crash of $\Delta I_{tot} \approx 0.5$ kA. The $v_\perp$ spike becomes significant at the PCR frequency steps of 30 to 33 GHz (corresponding to a cutoff density range of 1.12 to $1.35\times10^{19}\mathrm{m}^{-3}$), which means the crash event may be triggered at the limited radial position. By confirming the cutoff position on the Poincaré figure, the location of the $v_\perp$ spike occurs at the island boundary in the FMM configuration.

4.3. $v_\perp$ profile in the island region

In the EJM configuration, a 5/5 island chain intersects with the divertor plates, resulting in a 5/5 remnant island structure which holds for a good confinement property in the sea of open field lines[38]. The 5/5 island chain can be moderated by the control coil current, plasma current, and the edge plasma beta. At the mid-plane of the bean-shaped cross-section the remnant island can be captured by the PCR in the case that the island size is large enough. This allows the PCR to study the turbulence rotation in the island region.

Figure 10 presents the $v_\perp$ profile near the mid-plane island. The whole island structure is displayed by the Poincaré in dots, which is obtained by removing the divertor module in the FLT calculation. The remnant island can be seen in the connection length contour as its strength is colored by the grayscale. Here the $v_\perp$ is scaled to the PCR-A LoS for a better visualization in the island region, which is defined to be $v_{scaled} = v_\perp \times 10^{-5} - Z_{PCR-A}$. Thus the v_{scaled} above the PCR-A LoS represents a positive $v_\perp$ whereas the v_{scaled} below indicates a negative value. At $R \approx 6.23$ m the v_{scaled} starts to increase in all antenna combinations until it reaches to the maximum at $R \approx 6.22$ m. Then v_{scaled} decreases to its minimum at $R = 6.21$ m, where it is supposed to be the inner boundary of the island on the Poincaré figure. In the near-SOL region, the v_{scaled} increases again as the cutoff layer penetrates toward the LCFS.

It is observed that the v_{scaled} in BD combination is smaller than the others over the whole radial area, following with the v_{scaled} in BE. In the rest combinations, EC, DE, and DC are in a similar level in the island region. The different antenna combination indicates a distinct coverage to the remnant island structure in PCR measurements. However, the sign change of $v_\perp$ is not obvious when the remnant island size is small. As is shown in the figure 11(a), one can clearly see the scope of the $v_\perp$ changed between antenna combinations with B. And the $v_\perp$ value in BD is lower than the other combinations. In figure 11(b) the $v_\perp$ distribution depends on the perpendicular distance ($\Delta\xi_\perp$) in between. In BD combination $v_\perp$ is peaked at $v_\perp = 1.6$ km/s, which is related to the $\Delta\xi_\perp \approx 0.7$ cm, while in the BC combination, $\Delta\xi_\perp \approx 4.1$ cm and the peaked $v_\perp$ is up to 3.5 km/s in the island. The possible reasons for a smaller v_{scaled} of BD could be that, (i) the sight lines of B and D antennas are

localized above PCR-A toward the O-point of the island, while the E and C are more toward the X-point of the island. (ii) It is observed that the BD combination has a very broadband component in the coherence spectrum. As mentioned in section 3, the poloidal separation in BD is much shorter compared to the radial resolution. The τ_0 may be perturbed in this short distance measurement.

Moreover, the plasma current I_{tot} has an effect on the island rotation profile. Figure 12 explains how the $v_\perp$ profile in the island region evolves with the I_{tot}. The $v_\perp$ measurement in BD and EC combinations are presented as an example. As the I_{tot} ramping-up, the $v_\perp$ at both the inner and outer side of the island arises accordingly, and the width of the island expends in the $v_\perp$ profile. The $v_\perp$ gradient at the inner and outer boundaries of island becomes steep at higher I_{tot} level. This relation between $v_\perp$ and I_{tot} is also true for the EC combination (in figure12(b)). Note that the $v_\perp$ amplitude and its gradient are stronger than in BD combination. Moreover, there is no PCR measurement between R=6.212m and 6.223 m in I_{tot} = 4.26 kA case, which is because the peaked n_e profile in the island leads to a hollow region at the inner side of the island, where the PCR is unreachable due to its O-mode regime. The tuning point of $v_\perp$ at R $\approx$ 6.21 m is considered to be the inner boundary of the island, which moves inward from R = 6.215 m to R = 6.211 m as the I_{tot} increases. Besides, the $V_\perp$ in the near-SOL region increases from 0.6 km/s at I_{tot} = 0.65 kA to 1.4 km/s at 4.26 kA. However, the $v_\perp$ remains the same at the far-SOL region (R > 6.23 m).

5. Summary

To summarize the work, we introduce an EA model for the space-time correlation of the turbulence shear flow, and apply it to the $v_\perp$ estimation by mean of PCR measurement at the plasma edge of W7-X. The EA model shows a reasonable transition of the turbulence rotation in the shear layer, where the $v_\perp$ reverses the direction smoothly as the cutoff position moves through the shear layer. Studies are conducted under different configurations. (i) In the FTM configuration, $v_\perp$ gradient is inversely proportional to the ECRH heating power, which may be attributed to the turbulence activities near the plasma edge. (ii) The $v_\perp$ profiles are compared in the magnetic configuration scan. It shows a difference in the $v_\perp$ gradient between configurations. One interesting observation in the FMM configuration is that the $v_\perp$ spike occurs near the island boundary in response to the plasma current crash. (iii) In the standard configuration, the $v_\perp$ profile in different antenna combinations is observed to distribute with related to the $\Delta\xi_\perp$. Besides, the slope of $v_\perp$ evolves as the plasma current increases.

Acknowledgments

This work has been carried out within the framework of the EUROfusion consortium, and has received funding from the Euroatom research and training programme 2014-2018 and 2019-2020 under grant agreement No 633053, and was supported by the National Natural Science Foundation of China under Grant No. 11605235. The views and opinions expressed herein do not necessarily reflect those of the European Commission.

Reference

[1] Wolf R *et al.* 2017 *Nuclear Fusion* **57** 102020 URL http://stacks.iop.org/0029-5515/

57/i=10/a=102020

[2] Terry P W 2000 *Reviews of Modern Physics* **72** 109–165 ISSN 0034-6861 URL https://link.aps.org/doi/10.1103/RevModPhys.72.109

[3] Taylor G I 1938 *Proceedings of the Royal Society of London. Series A - Mathematical and Physical Sciences* **164** 476–490 ISSN 2053-9169 URL http://www.royalsocietypublishing.org/doi/10.1098/rspa.1938.0032

[4] Tal B, Bencze A, Zoletnik S, Veres G and Por G 2011 *Physics of Plasmas* **18** 37 ISSN 1070664X URL https://doi.org/10.1063/1.3662432

[5] Soldatov S, Krämer-Flecken A, Kantor M, Unterberg B, Sun Y, Van Oost G and Reiter D 2010 *Plasma Physics and Controlled Fusion* **52** 085001 ISSN 07413335 URL https://iopscience.iop.org/article/10.1088/0741-3335/52/8/085001

[6] Burrell K H 2020 Role of sheared e × B flow in self-organized, improved confinement states in magnetized plasmas URL https://doi.org/10.1063/1.5142734http://aip.scitation.org/doi/10.1063/1.5142734

[7] Prisiazhniuk D, Kramer-Flecken A, Conway G D, Happel T, Lebschy A, Manz P, Nikolaeva V and Stroth U 2017 *Plasma Physics and Controlled Fusion* **59** 025013 ISSN 13616587 URL https://iopscience.iop.org/article/10.1088/1361-6587/59/2/025013

[8] Krämer-Flecken A, Soldatov S, Xu Y and Zhang T 2011 *Plasma Physics and Controlled Fusion* **53** 074020 ISSN 0741-3335 URL https://iopscience.iop.org/article/10.1088/0741-3335/53/7/074020

[9] Nold B, Conway G D, Happel T, Müller H W, Ramisch M, Rohde V and Stroth U 2010 *Plasma Physics and Controlled Fusion* **52** 12 ISSN 07413335 URL https://iopscience.iop.org/article/10.1088/0741-3335/52/6/065005/pdf

[10] Nold B, Manz P, Ribeiro T T, Fuchert G, Birkenmeier G, Müller H W, Ramisch M, Scott B D and Stroth U 2014 *Physics of Plasmas* **21** 102304 ISSN 10897674 URL https://doi.org/10.1063/1.4897312http://aip.scitation.org/doi/10.1063/1.4897312

[11] Briggs B H, Phillips G J and Shinn D H 1950 *Proceedings of the Physical Society. Section B* **63** 106–121 ISSN 03701301 URL http://stacks.iop.org/0370-1301/63/i=2/a=305?key=crossref.cd326d7c8997b4b5177601a91728a97d

[12] He G, Jin G and Yang Y 2017 *Annual Review of Fluid Mechanics* **49** 51–70 (*Preprint* https://doi.org/10.1146/annurev-fluid-010816-060309) URL https://doi.org/10.1146/annurev-fluid-010816-060309

[13] Conway G D and Elliott J A 1987 *Journal of Physics E: Scientific Instruments* **20** 1341–1350 ISSN 0022-3735 URL https://iopscience.iop.org/article/10.1088/0022-3735/20/11/006

[14] Zhao X and He G W 2009 *Physical Review E - Statistical, Nonlinear, and Soft Matter Physics* **79** ISSN 15393755 URL https://journals.aps.org/pre/pdf/10.1103/PhysRevE.79.046316

[15] Sunn Pedersen T, König R, Jakubowski M *et al.* 2019 *Nuclear Fusion* **59** 096014 ISSN 17414326 URL https://doi.org/10.1088/1741-4326/ab280f

[16] Klinger T, Andreeva T, Bozhenkov S *et al.* 2019 *Nuclear Fusion* **59** 112004 ISSN 17414326 URL https://doi.org/10.1088/1741-4326/ab03a7

[17] Krämer-Flecken A, Windisch T, Behr W, Czymek G, Drews P, Fuchert G, Geiger J, Grulke O, Hirsch M, Knaup M, Liang Y, Neubauer O, Pasch E and Velasco J L 2017 *Nuclear Fusion* **57** 066023 ISSN 17414326 URL http://stacks.iop.org/0029-5515/57/i=6/a=066023?key=crossref.9b2cd1d0d667af56120ecbc5946add4e

[18] Windisch T, Krämer-Flecken A, Velasco J L, Könies A, Nührenberg C, Grulke O and Klinger T 2017 *Plasma Physics and Controlled Fusion* **59** 105002 ISSN 13616587 URL http://dx.doi.org/10.1088/1361-6587/aa759b

[19] Krämer-Flecken A, Han X, Windisch T, Cosfeld J, Drews P, Fuchert G, Geiger J, Grulke O, Killer C, Knieps A, Liang Y, Liu S and Rack M 2019 *Plasma Physics and Controlled Fusion* **61** 054003 ISSN 13616587 URL http://stacks.iop.org/0741-3335/61/i=5/a=054003?key=crossref.9582d77a3c16b40788f05da641dc1204

[20] Liang Y, Neubauer O, Konig R *et al.* 2017 *Nuclear Fusion* **57** 066049 ISSN 17414326 URL https://doi.org/10.1088/1741-4326/aa6cde

[21] Prisiazhniuk D, Conway G D, Krämer-Flecken A and Stroth U 2018 *Plasma Phys. Control. Fusion* **60** 75003 ISSN 13616587 URL http:

//dx.doi.org/10.1088/1361-6587/aabd0f

[22] Liu S C, Liang Y, Drews P, Krämer-Flecken A, Han X, Nicolai D, Satheeswaran G, Wang N C, Cai J Q, Charl A, Cosfeld J, Gao Y, Grulke O, Henkel M, Hollfeld K P, Killer C, Knieps A, König R, Neubauer O, Rack M, Sandri N, Sereda S, Schweer B, Wang E H and Wei Y L 2018 *Phys. Plasmas* **25** 72502 ISSN 10897674 URL https://doi.org/10.1063/1.5033353

[23] Carralero D, Estrada T, Windisch T, Velasco J L, Alonso J A, Beurskens M, Bozhenkov S, Damm H, Fuchert G, Gao Y, Jakubowski M, Nieman H, Pablant N, Pasch E and Weir G 2020 *Nucl. Fusion* **60** 106019 ISSN 17414326 URL https://doi.org/10.1088/1741-4326/ab9885

[24] Bozhenkov S A, Beurskens M, Molin A D *et al.* 2017 *Journal of Instrumentation* **12** ISSN 17480221 URL https://doi.org/10.1088/1748-0221/12/10/P10004

[25] Pasch E, Beurskens M N, Bozhenkov S A, Fuchert G, Knauer J and Wolf R C 2016 *Review of Scientific Instruments* **87** 11E729 ISSN 10897623 URL http://aip.scitation.org/doi/10.1063/1.4962248

[26] KrÄmer-Flecken A, Han X, Otte M, Anda G, Bozhenkov S A, Dunai D, Fuchert G, Geiger J, Grulke O, Pasch E, Scott E R, Trier E, VÉcsei M, Windisch T and Zoletnik S 2020 *Plasma Science and Technology* **22** 064004 ISSN 20586272 URL https://doi.org/10.1088/2058-6272/ab770c

[27] Han X, Kramer-Flecken A, Windisch T, Hirsch M, Fuchert G, Geiger J, Grulke O, Liu S and Rahbarnia K 2020 *Nuclear Fusion* **60** 016011 ISSN 17414326 URL https://iopscience.iop.org/article/10.1088/1741-4326/ab4e75

[28] Zoletnik S, Anda G, Aradi M, Asztalos O *et al.* 2018 *Review of Scientific Instruments* **89** 10–107 ISSN 10897623 URL https://doi.org/10.1063/1.5039309

[29] Wills J A 1964 *Journal of Fluid Mechanics* **20** 417–432 ISSN 14697645 URL https://www.cambridge.org/core/product/identifier/S002211206400132X/type/journal{_}article

[30] Burrell K H 1997 *Physics of Plasmas* **4** 1499–1518 ISSN 10897674 URL http://aip.scitation.org/doi/10.1063/1.872367

[31] Krämer-Flecken A, Soldatov S, Vowinkel B and Müller P 2010 *Rev. Sci. Instrum.* **81** 113502 ISSN 00346748 URL http://aip.scitation.org/doi/10.1063/1.3497305

[32] Soldatov S, Krämer-Flecken A and Klimov C N 2009 *Fusion Eng. Des.* **84** 64–71 ISSN 09203796 URL https://linkinghub.elsevier.com/retrieve/pii/S0920379608003426

[33] Zoletnik S, Anda G, Biedermann C *et al.* 2020 *Plasma Physics and Controlled Fusion* **62** 014017 ISSN 13616587 URL https://doi.org/10.1088/1361-6587/ab5241https://iopscience.iop.org/article/10.1088/1361-6587/ab5241

[34] Bozhenkov S A, Geiger J, Grahl M, Kißlinger J, Werner A and Wolf R C 2013 *Fusion Engineering and Design* **88** 2997–3006 ISSN 09203796 URL https://linkinghub.elsevier.com/retrieve/pii/S0920379613005711

[35] Rahbarnia K, Thomsen H, Neuner U *et al.* 2018 *Nuclear Fusion* **58** 096010 ISSN 0029-5515 URL https://doi.org/10.1088/1741-4326/aacab0https://iopscience.iop.org/article/10.1088/1741-4326/aacab0

[36] Andreeva T *et al.* 2020 *Nuclear Fusion* **under review**

[37] Wurden G A, Ballinger S, Bozhenkov S *et al.* 2018 Quasi-continuous low frequency edge fluctuations in the W7-X stellarator *45th EPS Conference on Plasma Physics, EPS 2018* vol 2-6 July 2 (Prague) p P5.107 ISBN 9781510868441 URL http://ocs.ciemat.es/EPS2018PAP/html/author.html

[38] Liu S C, Liang Y, Drews P *et al.* ISSN 17414326 URL https://iopscience.iop.org/article/10.1088/1741-4326/ab0d29

experimental ID	*Configuration name*	*Non-Planar Coil Currents* I_{1-5}(A)	*Planar Coil Currents* $I_{A,B}$(A)	$\iota/2\pi(0)$
180912048	FMM+252	13485	-4040	0.912
180912040	FOM+252	13608	-5040	0.928
180912034	FQM+252	13883	-7290	0.965
180912021	FTM+252	14219	-10040	1.012

Table 1. The coil currents setup in the magnetic configurations. The experimental IDs, configuration names according the W7-X internal specification, non-planar and planar coil currents, and the rotational transform value in the center volume of scanned configurations ($\iota/2\pi(0)$) are listed.

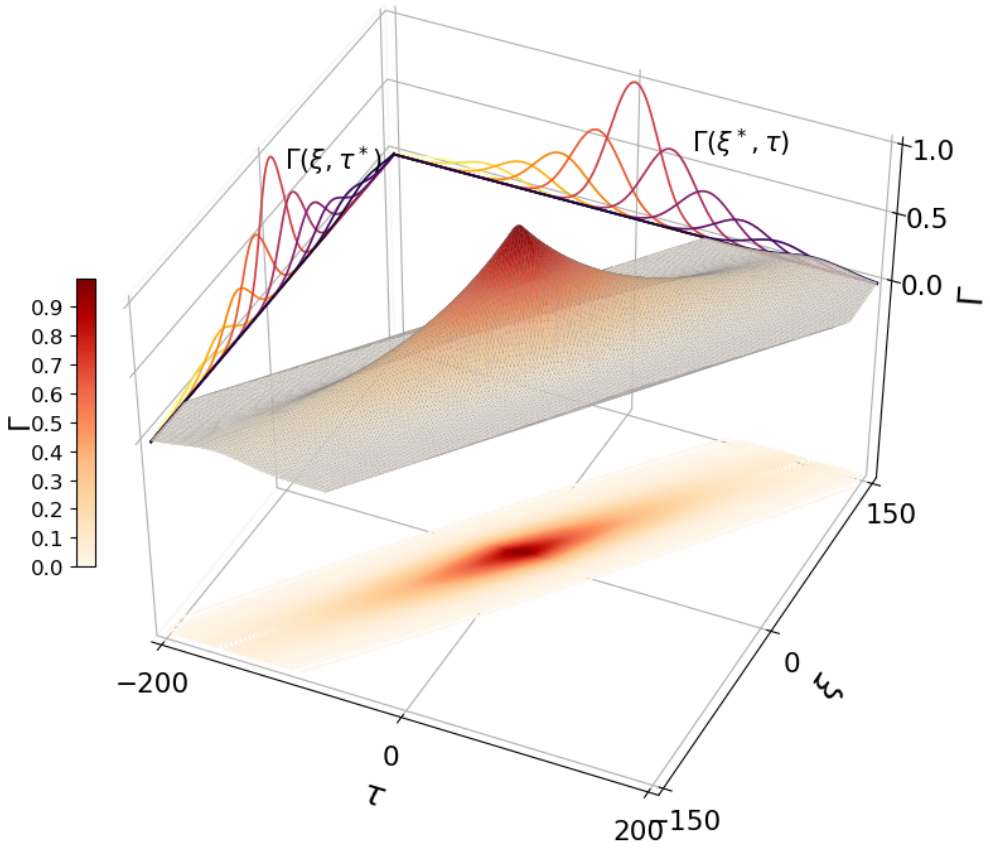

Figure 1. The turbulence flow as a function of space-time correlation in the shear layer.

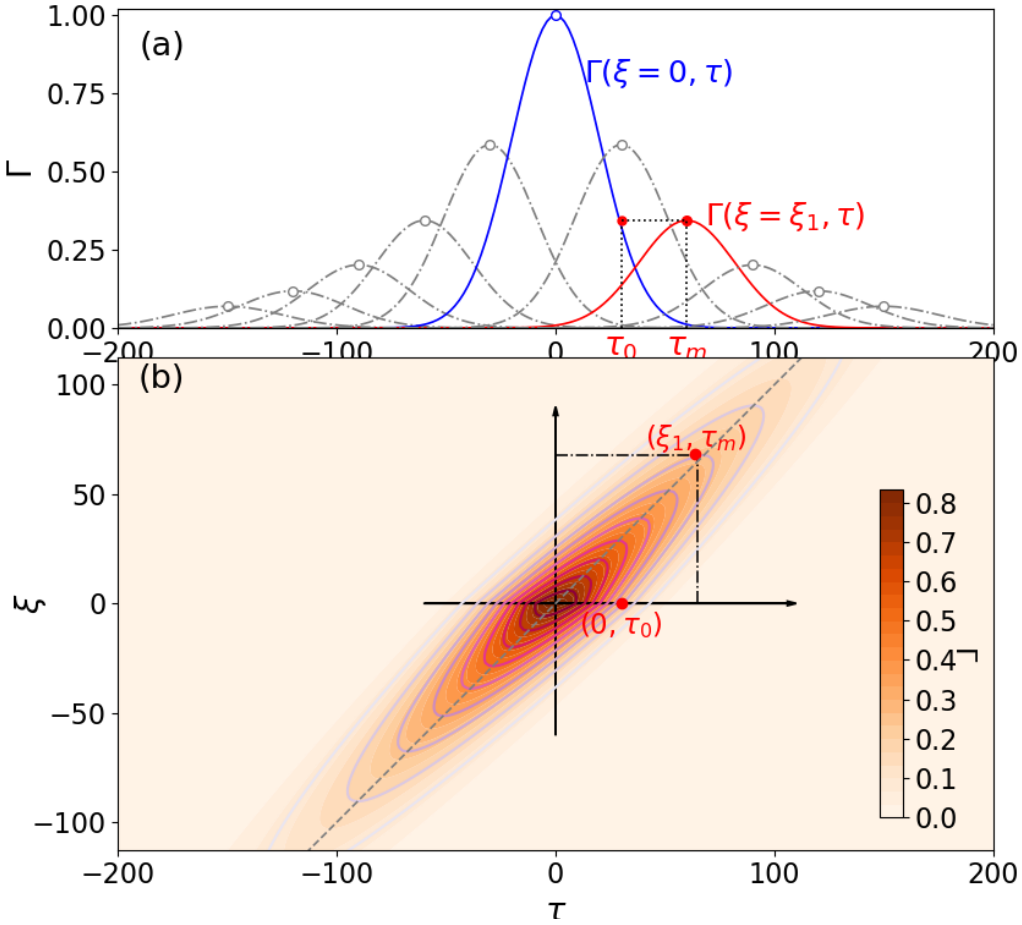

Figure 2. (a) The ACF (blue) and the CCF (red) at the space separation of ξ_1 distributions as a function of delay time. The grey dashed lines are the CCF in various space separations. (b) The iso-correlation contour of the turbulence flow in the shear layer. The grey dahsed line indicates the preference direction of the ellipse, and the colorbar shows the correlation coefficient of the turbulence eddy.

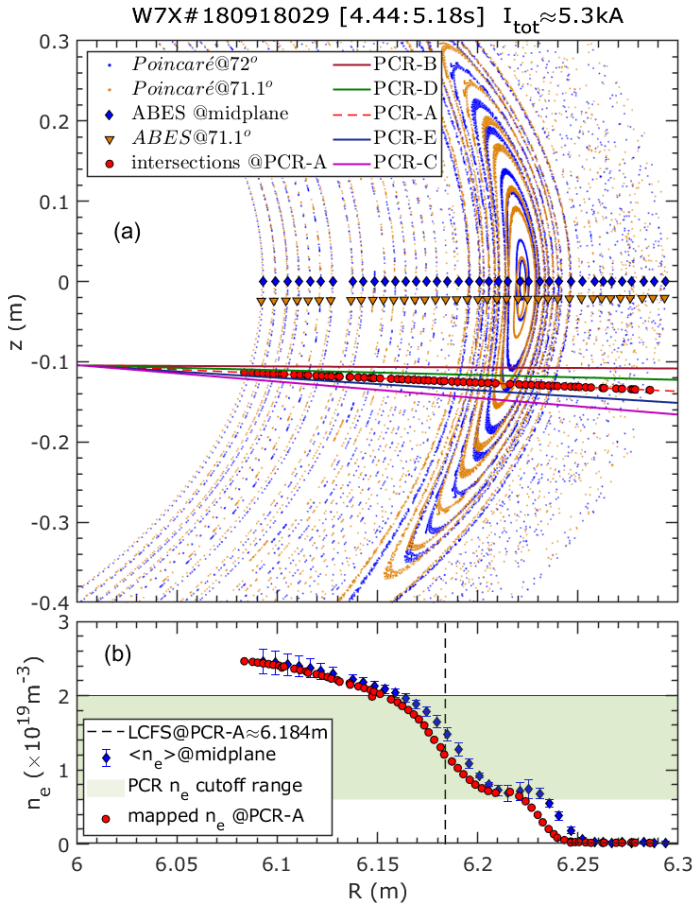

Figure 3. (a) The Poincaré plots in the toroidal angle of 72° (blue dots) and 71.1° (yellow dots) corss-sections. The orignal ABES measurements are labeled as the blue diamonds on the equatorial plane. The yellow triangles are the corresponding points at the PCR cross-section by tracing the field lines from ABES to PCR. The red dashed line is the PCR launcher LoS (labeled as PCR-A), and the four receivers LoS are indicated as the bold lines in different colors. The red dots on PCR-A are the intersections in each of the fluxsurface of 71.1°. (b) The n_e profile at the mid-plane (blue) and the PCR-A LoS (red). The errorbar in blue indicates the density variation within the PCR sweep cycle. The vertical dashed line shows the location of the LCFS along the PCR-A LoS.

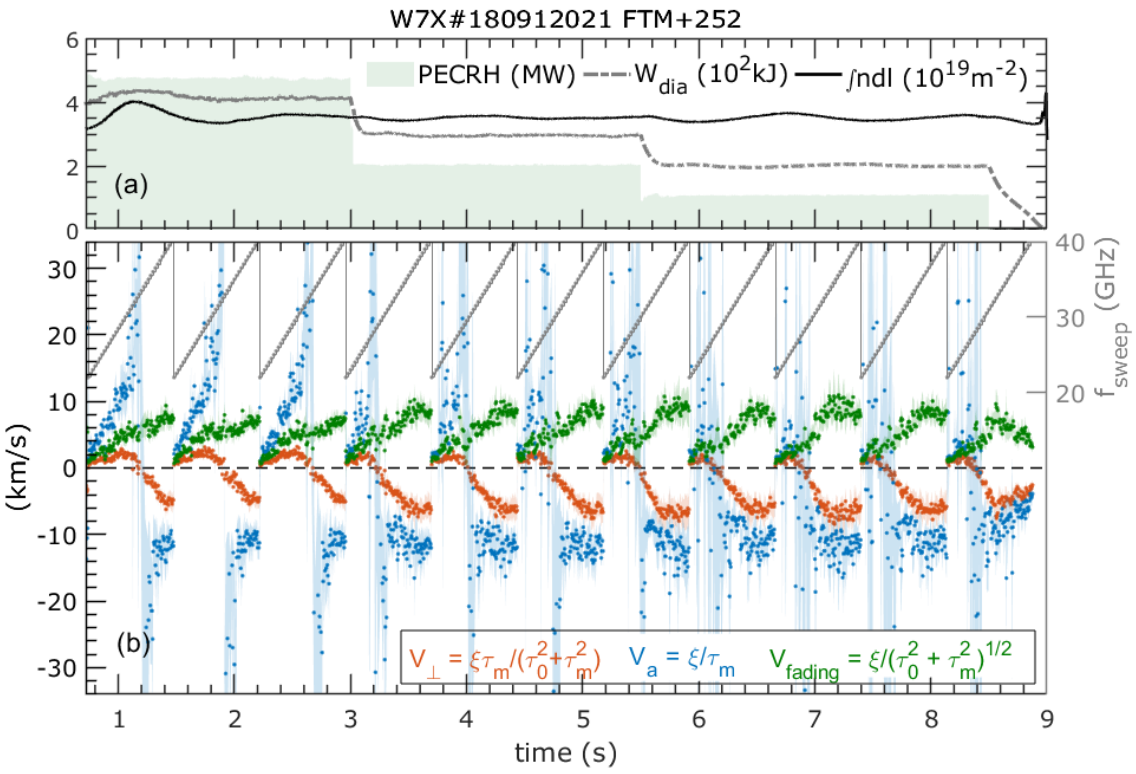

Figure 4. (a) Time traces of diamagnetic energy (grey dashed line) and the line-integrated density (black line). The ECRH power level is shown in the green bar. (b) Time traces of $v_{\perp}$, v_a, and v_{fading}. The PCR sweep cycle is presented in the grey color on the right vertical axis.

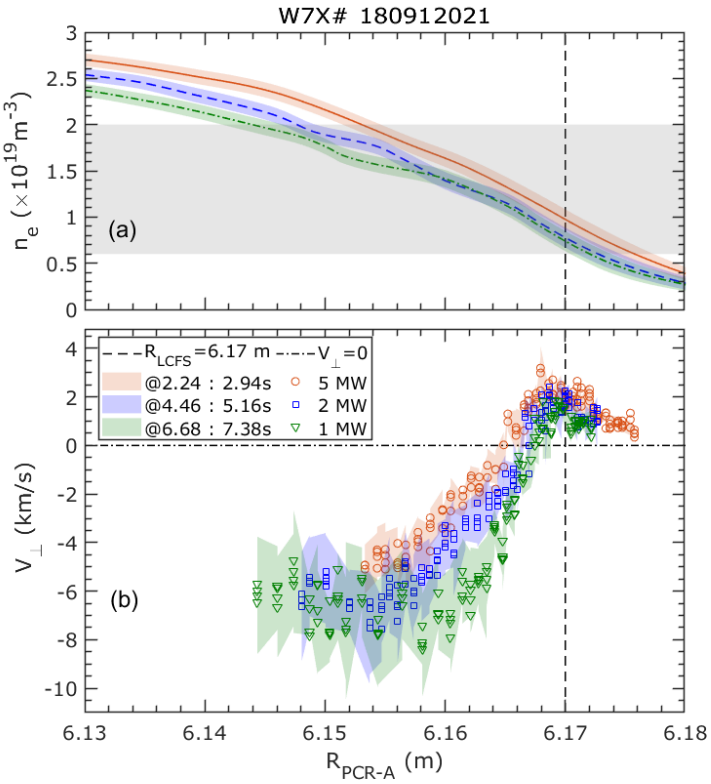

Figure 5. (a) Electron density profiles in different ECRH powers. The color range indicates the density variation within the PCR sweep cycle. (b) The $v_\perp$ profiles in each of the ECRH power step. The vertical dashed line shows the location of the LCFS along the PCR-A LoS.

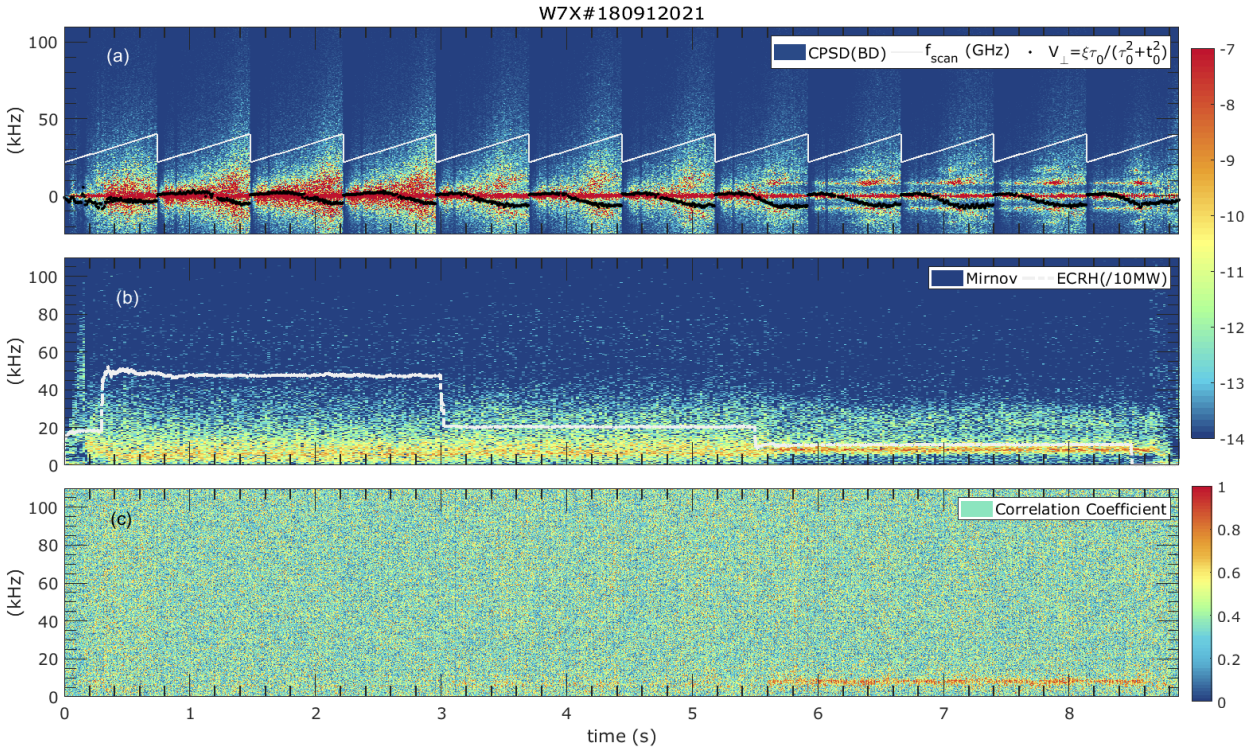

Figure 6. (a) CPSD of BD combination. The PCR sweep cycle is indicated as the white dot, and the $v_\perp$ evolution is shown with the black dot. (b) The magnetic fluctuation spectrum, the white line shows the ECRH heating power. (c) The correlation coefficient between the PCR-B and Mirnov signals.

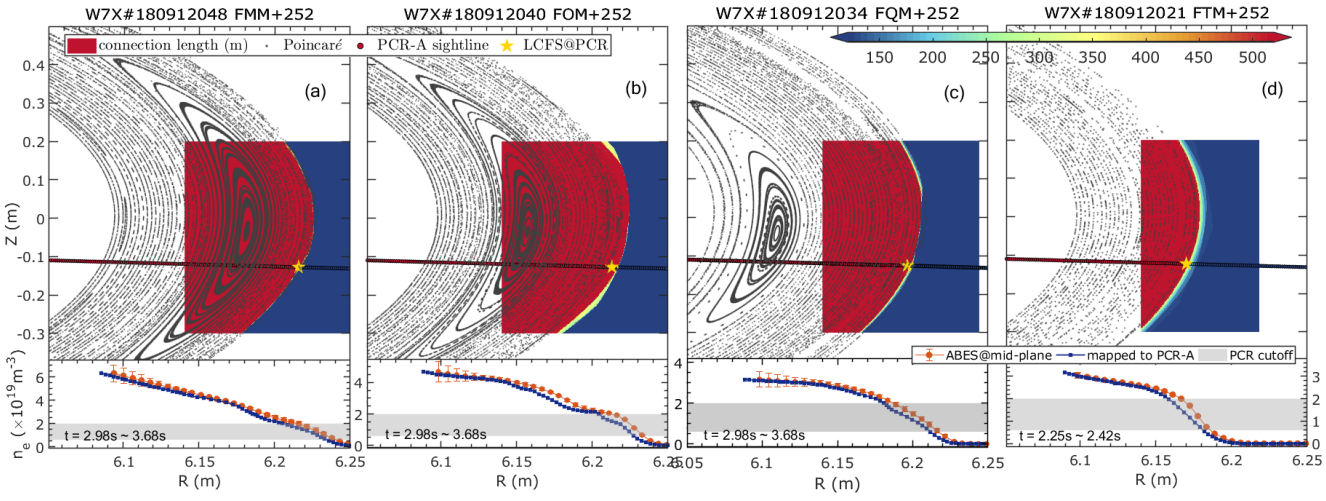

Figure 7. The Poincaré plot (black dot) with the connection length contour (in color) in the magnetic configuration of (a) FMM+252, (b) FOM+252, (c) FQM+252, and (d) FTM+252. The PCR-A sightline is indicated by the red dots. The yellow star shows the LCFS along PCR-A sightline individually. The n_e profiles of ABES (red dot) and PCR (blue dot) are shown below each of the Poincaré figure accordingly. The grey area indicates the cutoff density range of PCR.

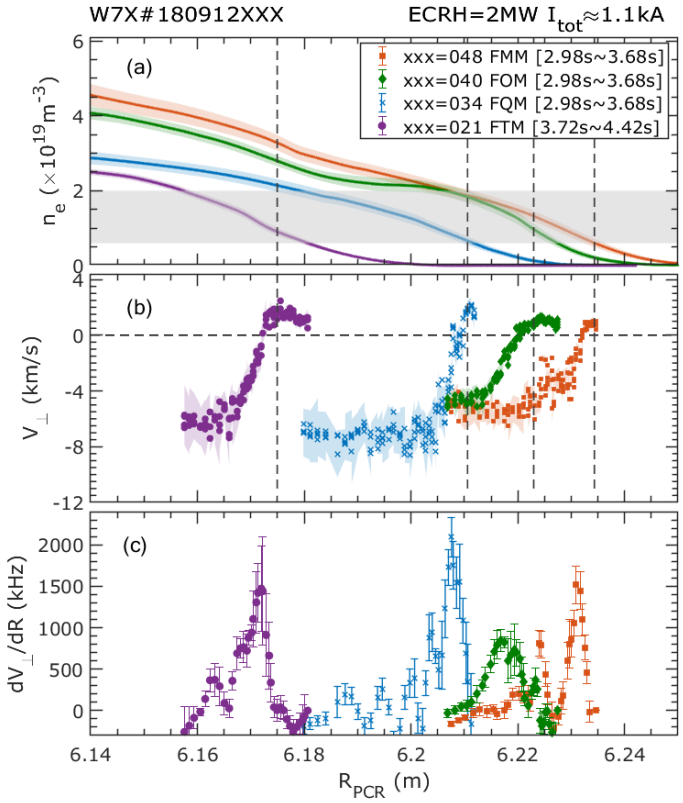

Figure 8. (a) n_e profiles in the configuration scan. The color range shows the variation of the n_e within the PCR sweep cycle. The grey area indicates the cutoff density range of PCR. (b) $v_\perp$ profiles for each discharge with the same color order of (a). (c) The $v_\perp$ gradient profiles with respect to discharges in the same color order. The vertical dashed line in (a) and (b) shows the LCFS on PCR-A LoS in each discharge.

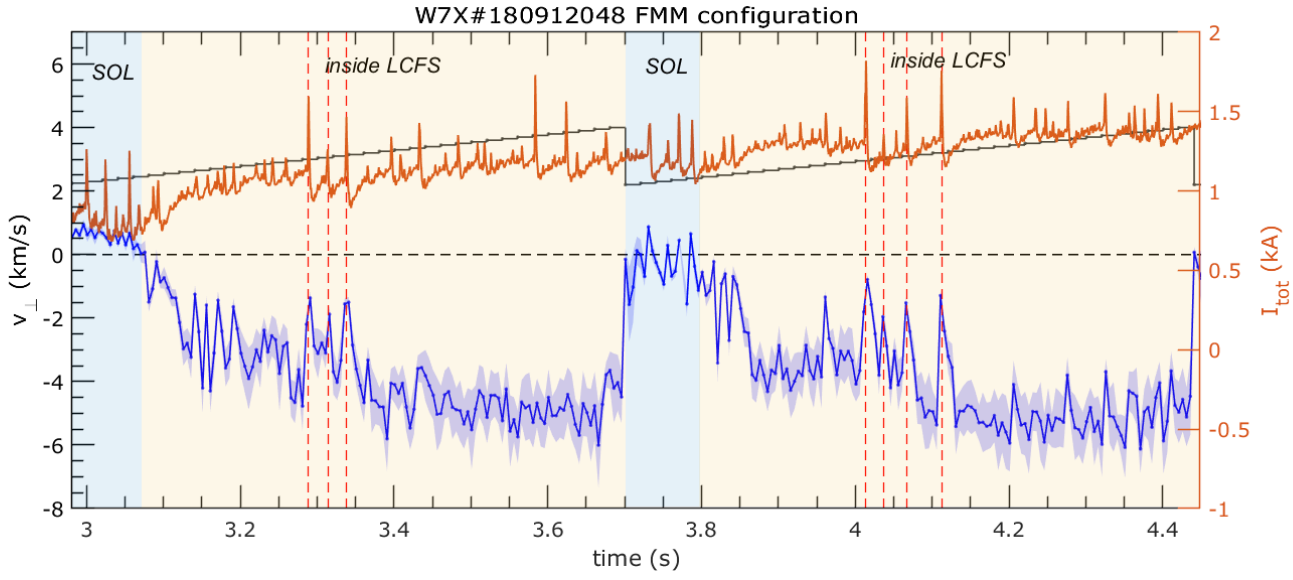

Figure 9. The time traces of $v_\perp$ (blue), I_{tot} and the PCR sweep frequency (black dots). The blue and yellow areas show the time window of SOL and inside the LCFS individually.

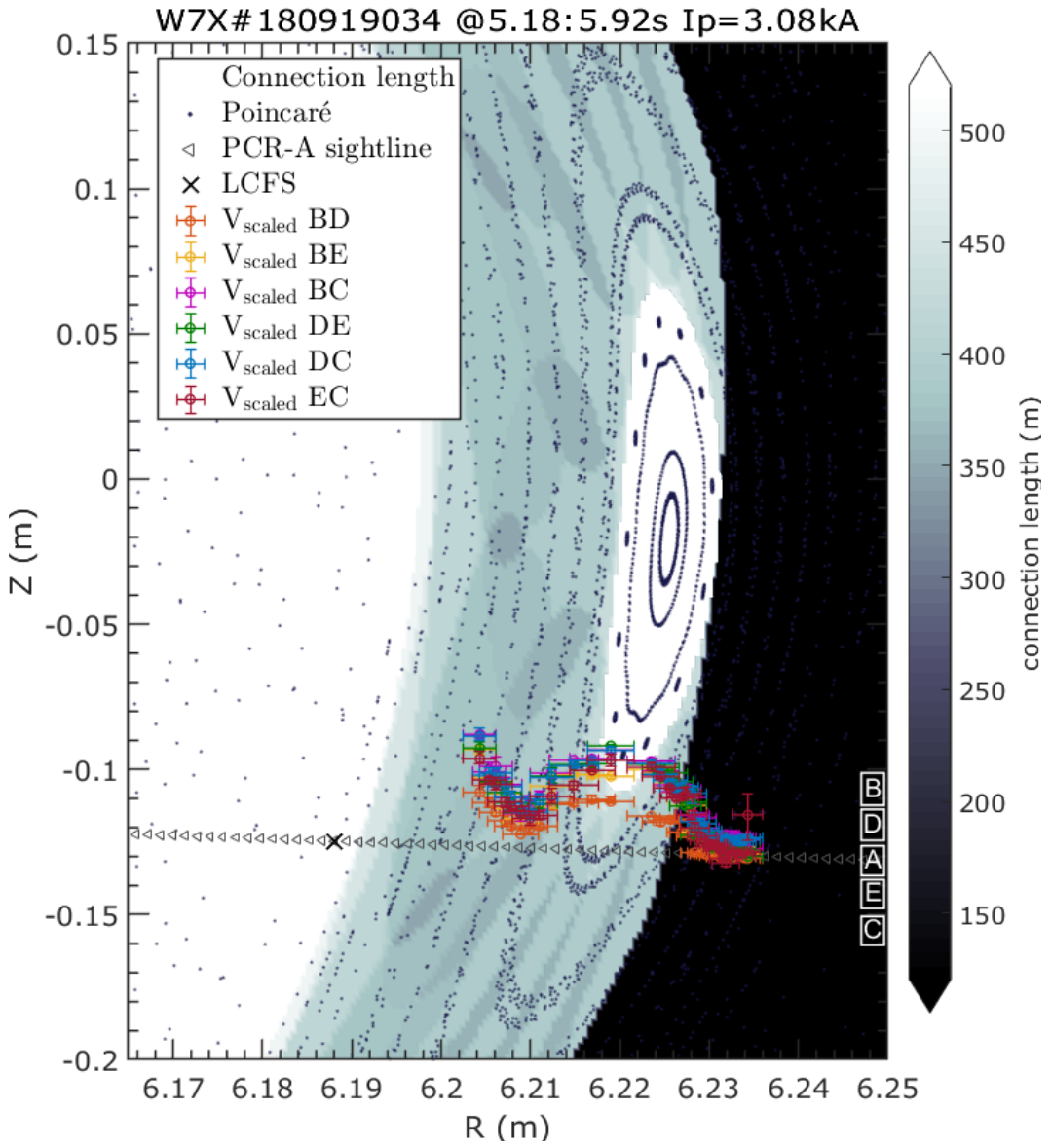

Figure 10. The v_{scaled} on the PCR-A LoS for all the antenna combinations as indicated by with the colors. The Poincaré plot is shown by the grey dots. The connection length contour is overlapped with its strength indicated by the shade of gray. The LoS of PCR-A is shown as the triangles, and the locations of the PCR antenna array are indicated by the letters on the right side. The LCFS position is located at the black cross on the PCR-A LoS.

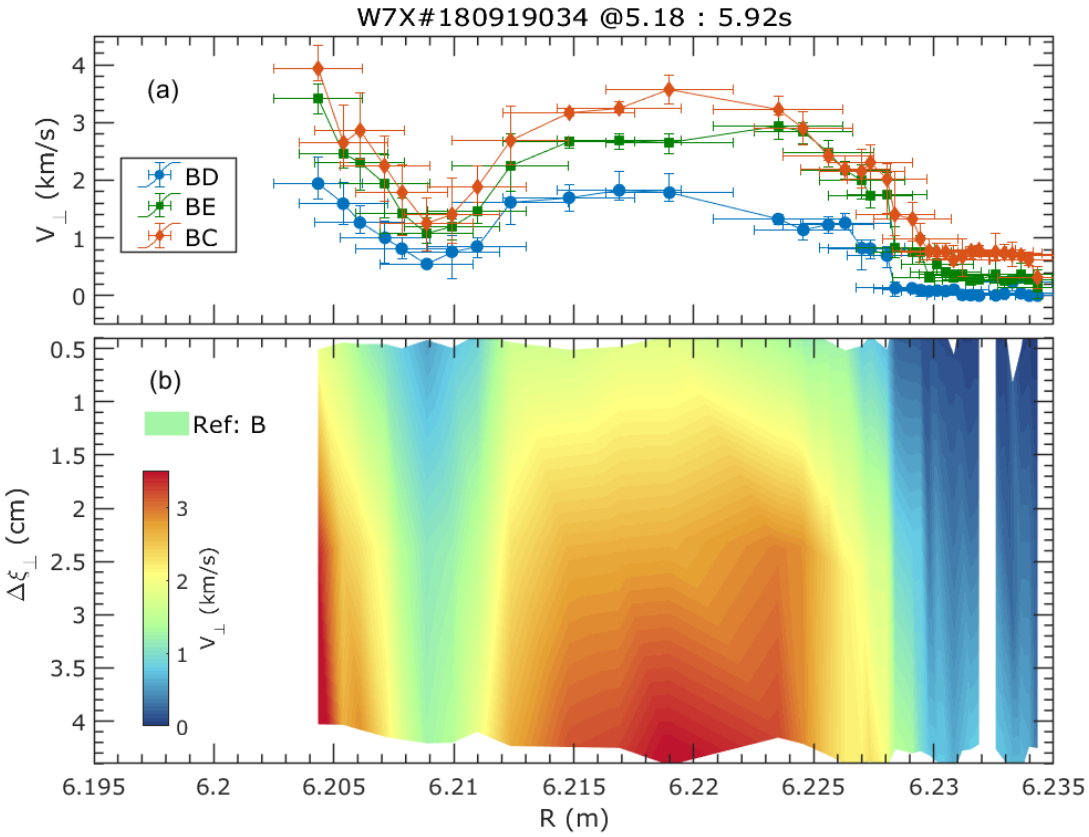

Figure 11. (a) $v_\perp$ profiles in BD (blue), BE (green), and BC (yellow) combinations. (b) The contour of $v_\perp$ as a function of the perpendicular distance ($\Delta s_\perp$) referenced to antenna B. The area beyond the $\Delta s_\perp$ is filled in white. The $v_\perp$ value is labeled by the colorbar.

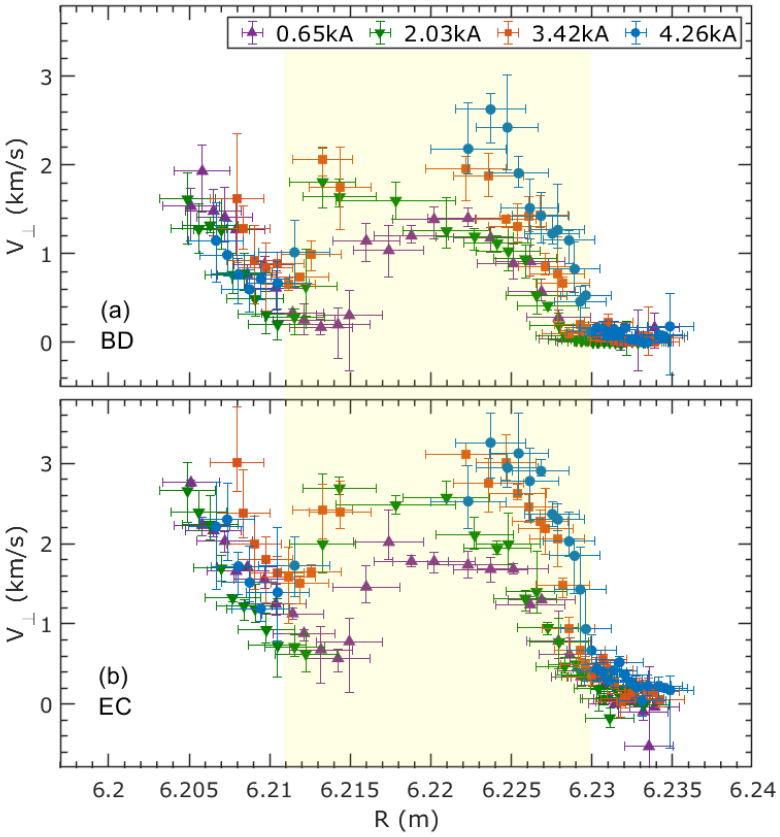

Figure 12. $v_\perp$ profiles in (a) BD and (b) EC combinations. The colors with symbols indicate the measurement of different I_{tot}. The light yellow region shows the radial extend of remnant island.